ACS APPLIED MATERIALS & INTERFACES

Research Article

www.acsami.org

Reduced-Graphene Oxide/Poly(acrylic acid) Aerogels as a Three-Dimensional Replacement for Metal-Foil Current Collectors in Lithium-Ion Batteries

Han Xiao,[†] Joshua P. Pender,[‡] Mackenzie A. Meece-Rayle,[‡] J. Pedro de Souza,[†] Kyle C. Klavetter,[†] Heonjoo Ha,[†] Jie Lin,[†,§] Adam Heller,[†] Christopher J. Ellison,*[,†] and C. Buddie Mullins*[,†,‡]

[†]John J. McKetta Department of Chemical Engineering and [‡]Department of Chemistry, The University of Texas at Austin, Austin, Texas 78712, United States

[§]Pen-Tung Sah Micro-Nano Science and Technology Institute, Xiamen University, Xiamen, Fujian 361005, China

Supporting Information

ABSTRACT: We report the synthesis and properties of a low-density (~5 mg/cm^3) and highly porous (99.6% void space) three-dimensional reduced graphene oxide (rGO)/poly(acrylic acid) (PAA) nanocomposite aerogel as the scaffold for cathode materials in lithium-ion batteries (LIBs). The rGO-PAA is both simple and starts from readily available graphite and PAA, thereby providing a scalable fabrication procedure. The scaffold can support as much as a 75 mg/cm^2 loading of $LiFePO_4$ (LFP) in a ~430 μm thick layer, and the porosity of the aerogel is tunable by compression; the flexible aerogel can be compressed 30-fold (i.e., to as little as 3.3% of its initial volume) while retaining its mechanical integrity. Replacement of the Al foil by the rGO-PAA current collector of the slurry-cast LFP (1.45 ± 0.2 g/cm^3 tap density) provides for exemplary mass loadings of 9 mg_{LFP}/cm^2 at 70 μm thickness and 1.4 g/cm^3 density or 16 mg_{LFP}/cm^2 at 100 μm thickness and ~1.6 g/cm^3 density. When compared to Al foil, the distribution of LFP throughout the three-dimensional rGO-PAA framework doubles the effective LFP solution-contacted area at 9 mg/cm^2 loading and increases it 2.5-fold at 16 mg/cm^2 loading. Overall, the rGO-PAA current collector increases the volumetric capacity by increasing the effective electrode area without compromising the electrode density, which was compromised in past research where the effective electrode area has been increased by reducing the particle size.

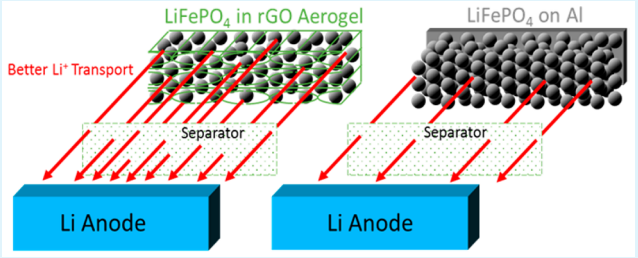

KEYWORDS: *reduced graphene oxide, aerogel, 3D nanoarchitecture, cathode, lithium-ion battery, nanocomposite*

1. INTRODUCTION

Rechargeable lithium-ion batteries (LIBs) power most of the portable electronic systems and are increasingly used in electric cars.[1−4] Metrics for the improvement of their electrodes include the achievable volumetric and gravimetric energy and power densities and the cyclability. While the active-material specific capacities and rates can be high, the electrodes' actual specific capacities and rates are often limited by their high content of inactive materials, such as current-collector foils, conductive additives, and polymeric binders. One of the several ways to alleviate such a limitation is to increase the effective surface area of the electrode. In doing so, the electrode−electrolyte contact area is increased and the kinetics for Li insertion/deinsertion are improved. In addition, pores that are not excessively tortuous can be engineered for rapid diffusional electrolyte influx and outflux even in a nonflowing electrolyte. If particles are distributed effectively and the desired pore structure is achieved in free-standing, flexible, mechanically strong, and electrically conductive electrodes with thick electroactive layers, an increase in volumetric energy density with adequate transport for at least moderate rates would be coupled to a reduction in production costs of stacked-electrode rectangular cells and rolled-electrode cylindrical cells. However, the mechanical and transport properties of today's electrode materials preclude film thicknesses greater than about 100 μm.[4−6]

Simultaneous achievement of a material with high specific capacity at a high rate and good cycling stability rarely leads to commercially viable electrodes[7−9] either because of the cost of the often nanoscale materials or because their loading is ≲3 mg/cm^2.[10−13] Nanoscale intercalation materials with short intragrain Li^+ diffusion distances provide smooth rather than rough electrode surfaces: as the particle size shrinks, the coated surface becomes smoother, reaching perfect smoothness at the atomic-size limit. As the electrochemically active surface area increases with surface roughness, increasing the effective area of small-particle loaded electrodes has been an important target of LIB electrode research.[12−21] 3-D electrode architectures and

Received: May 23, 2017
Accepted: June 20, 2017
Published: June 20, 2017

DOI: 10.1021/acsami.7b07283
ACS Appl. Mater. Interfaces 2017, 9, 22641−22651

substrates can provide LIB electrodes with thicker electroactive films that can have a high effective solution-contacting area when their pores are engineered for adequate diffusional ion influx and outflux in the nonflowing electrolytic solutions of LIBs. Some 3-D electrodes made with graphene show promise because of their mechanical stability and electronic conductivity.[22−28] Progress in graphene-comprising LIB electrode research has been enormous in the past decade: graphene is a superior conductive additive[29] in composites with active materials[30−32] forming a conductive network.[33] Notably, Zhou et al. used a nitrogen/sulfur codoped graphene sponge electrode as a substrate in a lithium−sulfur battery showing high capacity retention after 500 cycles.[34] However, graphene-based materials are expensive, and their low mass loading of ≤3 mg/cm^2 has hindered widespread adoption of these materials in LIBs.

To reduce the cost and to increase the mass loading, we introduce here a thermally cross-linked, reduced graphene oxide−poly(acrylic acid) (further referred as rGO-PAA) aerogel as a high specific surface area current collector. The thermally cross-linked structure of PAA on graphene oxide (GO) sheets make the aerogel elastic and robust;[35] it can be compressed without fracturing, and its electrical conductivity is $(5.3 \pm 3) \times 10^{-2}$ S/m. Its synthesis is simple, and the cost of its starting materials, graphite and PAA, is lower than that of most other starting materials used for making LIB components.

The potential utility of carbon-based 3-D materials in LIBs has been recognized.[32,34,36−51] Metal oxide/aerogel anode nanocomposites have been made with Fe_2O_3 nanoparticles,[42] spinel $ZnMn_2O_4$ nanocrystals,[43] and Co_3O_4 nanoparticles[44] and with carbon itself.[45] 3-D cathodes have been fabricated with carbon aerogels and SeS_2 nanoparticles[46] and $LiFePO_4$ nanoparticles.[32,47,48] Lithium−sulfur battery cathodes were made using monoclinic sulfur,[49] amorphous TiO_2/sulfur,[50] and CeO_2 nanoparticles[51] loaded onto carbon aerogels. 3-D and porous carbons have also been used as scaffolds for sulfur trapping in sulfur cathodes.[52−56] In these studies, faster charge/discharge rates, longer cycle life, or improved capacity retention were simultaneously achieved, but researchers have often neglected to consider the mechanical properties, fabrication costs, or volumetric energy densities of the electrodes. In some studies, expensive metal precursors were used; in others, the materials required multistep syntheses; and yet others yielded fragile aerogel composites, making their manufacture and use difficult. These issues are addressed here through the free-standing and mechanically robust rGO-PAA current collector. The $LiFePO_4$ (LFP) is slurry cast onto the rGO-PAA aerogel substrate. The high theoretical capacity of LFP (170 mAh/g) coupled with its relatively low cost and its environmental compatibility are increasing the use of LFP in LIBs.[15,16] We use commercially produced, 3.5 ± 1 μm mean-particle diameter and 1.45 ± 0.2 g/cm^3 tap-density LFP.[15] Unlike the earlier LFPs which required carbon-coating to improve their electronic and Li^+ transport kinetics,[17,18] or required particle size reduction to improve the rate capability at the expense of reducing the tap density in nano-LFP to ≤1.0 mg/cm^3,[19,20] the LFP slurry cast onto rGO-PAA is not modified and a high-tap density LFP is retained for high volumetric capacity.[15−21]

The depth of the effectively utilized part of the rGO-PAA-LFP layer depends on the diffusion lengths of the incoming and outgoing ions, which scale with the square root of the residence time and decreases with the inverse of the current density. The effective electrolyte penetration depth into the 3-D aerogel depends on the tortuosity of the pores, with straight through pores offering the shortest paths and being the most penetrable. The effectively utilized depth, i.e., the depth to which the concentration polarization decreasing the operating voltage is not excessive, shrinks with the inverse of the square root of the current density. The rGO-PAA aerogel current collector is not excessively tortuous and is advantageous over metal foils because of its much lower density of ∼5 mg/cm^3 vs 2700 mg/cm^3 for Al foil and 8940 mg/cm^3 for Cu foil. Another attractive combination of properties includes the highly porous ∼99.6% void space of the rGO-PAA that allows large electrolyte permeation through its nontortuous pores, coupled with its mechanical durability, exemplified by its ability to withstand 30-fold compression without fragmentation.

In this study, a commercial LFP of high tap density was slurry-cast onto rGO-PAA and onto Al foil (further referred to as LFP-rGO and LFP-Al) and calendered to thicknesses of ∼70 μm (LFP = 9 mg/cm^2) and ∼100 μm (LFP = 16 mg/cm^2). The active material weight fraction in the LFP-rGO electrodes was ∼79 wt % at 70 μm thickness and ∼85 wt % at 100 μm thickness, higher than the ∼68 and ∼74 wt % in the corresponding LFP-Al electrodes. The LFP content of the LFP-rGO electrode also exceeded the ∼64 wt % content of the ultrathin graphene foam composite of Ji et al.[36] and the ∼70 wt % content of commercial LFP on Al cathodes sold by MTI Corporation (see the Supporting Information). Overall, the low density of rGO-PAA versus that of aluminum reduced the weight of the electrode, and the distribution of LFP throughout the 3-D framework increased the amount of LFP loaded per unit area at a given film thickness. The wettability of rGO-PAA provided for uniform and reproducible LFP loadings from simple slurry casting, allowing for the more difficult coprecipitation and hydrothermal methods of forming composite electrodes to be avoided.[29−34,37−51] The 3-D rGO-PAA framework with engineered pores increases both the electrolyte-accessed surface area and the rapid permeation through the electrode at a given thickness, providing for an electrochemical advantage over electrodes made with aluminum or copper substrates.

2. EXPERIMENTAL SECTION

2.1. Materials. All chemicals were used as-received unless otherwise noted. Sulfuric acid (H_2SO_4; 90%), potassium permanganate ($KMnO_4$), hydrogen peroxide (H_2O_2; 30%), and hydrochloric acid (HCl) were purchased from Fisher Scientific to prepare graphene oxide (GO). GO samples were synthesized exactly as described in a previous paper, which also reported their mechanical properties.[35] Preoxidized graphite was purchased from Bay Carbon Inc. (SP-1) and used to synthesize GO. Poly(acrylic acid) (PAA) with a viscosity average molecular weight (M_v) of 450 000 was purchased from Sigma-Aldrich. Hydroiodic acid (HI; 55%) was purchased from Sigma-Aldrich and used to reduce GO. Sylgard 184 silicone elastomer was purchased from Dow Corning to prepare molds for rGO-PAA. Lithium was provided by Alfa and used as the anodes for all cells. Lithium iron phosphate ($LiFePO_4$) and Super P were purchased from MTI Corporation. Styrene−ethylene−butylene−styrene block copolymer (Kraton G1652 M, Kraton Polymers) was used as a binder for active materials. Toluene was purchased from Fisher Scientific. Lithium hexafluorophosphate ($LiPF_6$; 99.99%) and diethyl carbonate (DEC; 99%) were purchased from Sigma-Aldrich, and ethylene carbonate (EC) was purchased from EMD Chemicals. Celgard 2400 microporous monolayer membranes (polypropylene, 25 μm) were generously supplied by Celgard.

2.2. Synthesis of Aerogel Molds. Polydimethylsiloxane (PDMS) elastomers and curing agents from a Sylgard 184 Silicone Elastomer

DOI: 10.1021/acsami.7b07283
ACS Appl. Mater. Interfaces 2017, 9, 22641−22651

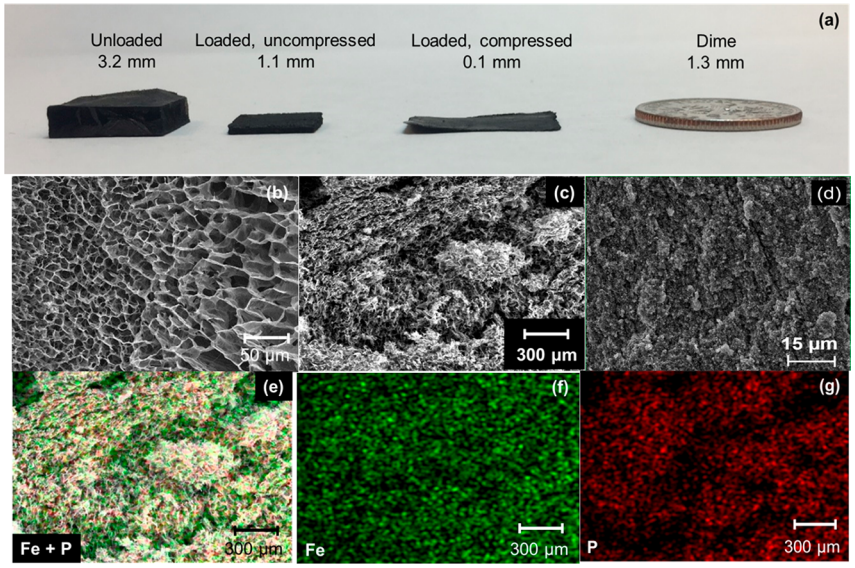

Figure 1. (a) From left to right: a pristine rGO-PAA aerogel; rGO-PAA aerogel loaded with LFP particles but not compressed by calendering (the thickness decreased because the substrate was dried under slight mechanical pressure to avoid curling of the sample because of uneven drying rates at its edges); a loaded and compressed by calendering the rGO-PAA electrode; a US dime as a reference. (b) SEM image of the cross section of the pristine rGO-PAA aerogel with no LFP/Super P Li. (c) SEM image of the cross-section of rGO-PAA loaded with LFP (~16 mg/cm^2) and Super P Li after drying under slight mechanical pressure. (d) SEM image of the cross section of rGO-PAA loaded with LFP/Super P Li and compressed by calendering (LFP loading = 16 mg/cm^2; 100 μm thickness). (e) Cross-sectional EDS of the compressed electrode. Green is iron and red is phosphorus. (f) Iron elemental mapping. (g) Phosphorus elemental mapping.

Kit were well-mixed at the recommended 10:1 ratio in a polystyrene Petri dish. Two acrylonitrile−butadiene−styrene copolymer bars (ABS; 60 mm × 12.7 mm × 3.2 mm) were placed on top of the elastomer mixture to make the bar-shaped templates, and then the Petri dish was transferred to a room temperature vacuum oven at ~5 in Hg for 1 h to remove any air bubbles. Afterward, the samples were moved to an oven at 60 °C for 4 h to cure the elastomer. The molds were obtained by removing the ABS template bars from the cured PDMS.

2.3. Synthesis of GO-PAA Aerogels. GO-PAA aerogels were synthesized according to a previous report[35] with a few modifications. PAA (25 mg) was added to 10 mL of deionized water (DI water) in a 20 mL scintillation vial. The mixture was stirred at 1000 rpm for 10 min until all PAA was visibly dissolved. GO (50 mg) was introduced to the solution and stirred at 2500 rpm for 20 min until all GO was visibly dissolved/dispersed. The solution was sonicated using a 400 W probe sonicator (1/8 in. probe; Branson Digital Sonifier 450) with 10% amplitude for 10 min (24 kJ) in an ice bath to fully exfoliate GO and promote a homogeneous solution. The PDMS molds were transferred to a Pyrex Petri dish, and the GO-PAA aqueous solution was transferred to the molds. The sample was freeze-dried by immersing in liquid nitrogen for 5 min and then pulling vacuum at room temperature for 24 h.

2.4. Synthesis of rGO-PAA Aerogels. The GO-PAA aerogels from the previous step were placed in a glass chamber containing HI vapor at room temperature for 24 h to reduce GO. The rGO-PAA samples were then moved to a vacuum oven and annealed at 160 °C for 24 h to remove residual HI molecules and thermally cross-link PAAs to poly(acrylic anhydrides). The average rGO-PAA aerogel density was 5 mg/cm^3 with a porosity of 99.6%, as described in a previous report.[35]

2.5. Construction of LFP-rGO Cathodes. LFP-rGO electrodes were fabricated by mixing LFP, Super P, and Kraton in a 92.5%:5%:2.5% mass ratio in toluene solvent. The particles were dispersed in the solvent by stirring at 1000 rpm for 10 min and then sonicating using a 400 W probe sonicator (1/8 in. probe; Qsonica Q500) with 20% amplitude for 15 min (36 kJ) in an ice bath. The slurry was rapidly introduced into rGO-PAA by directly pouring onto the aerogel and allowing the rGO-PAA to soak in the slurry for about 1 min. After removing the rGO-PAA substrate coated with active materials from the slurry bath, the substrate was gently rolled on a filter paper to remove residual slurry coating the outer substrate surfaces. The substrates were then placed under slight mechanical pressure to prevent the substrate from curling up because of uneven drying rates at its edges. The aerogel sample was dried under vacuum at 80 °C for 16 h, compressed to the desired thickness with a calender (MRX-SG100L, Polaris Battery Laboratories), and cut to coin-cell compatible cathodes (0.1−0.3 cm^2) with a razor blade. A cartoon scheme for making LFP-rGO electrodes can be found in the Supporting Information (Figure S1).

2.6. Construction of LFP-Al Cathodes. LFP-Al electrodes were fabricated by mixing LFP, Super P, and Kraton in a 92.5%:5%:2.5% mass ratio in toluene solvent. The particles were stirred at 1000 rpm for 10 min and then sonicated using a 400 W probe sonicator (1/8 in. probe; Qsonica Q500) with 20% amplitude for 15 min (36 kJ) in an ice bath. The slurry was then cast onto Al-foil (Alfa Aesar), dried under vacuum at 80 °C for 16 h, calendered to the desired thickness, and hole-punched into individual electrodes (7/16 in. diameter disk).

2.7. Characterization of LFP-rGO Cathodes. Scanning electron microscopy (SEM; FEI Quanta 650 ESEM) was used to examine the morphology of the cross section of all materials. Energy dispersive spectroscopy (EDS; Hitachi S5500) was used to observe the elemental dispersion on the cross section. The cross section of the electrodes was examined using cryo-fractured samples. Because of the sufficiently high electrical conductivity of the aerogel after reduction,[35] the sample was examined without any additional presample treatment.

2.8. Electrochemical Tests of Cathodes. An electrochemical analyzer (CHI 608D, CH Instruments) was used for cyclic voltammetry (CV) and electrochemical impedance spectroscopy (EIS). CV was performed over a potential range of 2.5−4 V with a scan rate of 0.1 mV/s for all tests. EIS was measured over a frequency range from 0.01 Hz to 100 kHz. Four-point probe measurements of the pristine rGO-PAA substrate were conducted on a manual four-point resistivity probe (Lucas S302; Lucas Laboratories) to measure the sheet resistance of the rGO-PAA substrate. The potential was stepped from −1.5 to 1.5 V in 500 mV increments, and the current was recorded at each value. The sheet resistivity was then calculated via a modified ohm's law and is described in the Supporting

DOI: 10.1021/acsami.7b07283
ACS Appl. Mater. Interfaces 2017, 9, 22641−22651

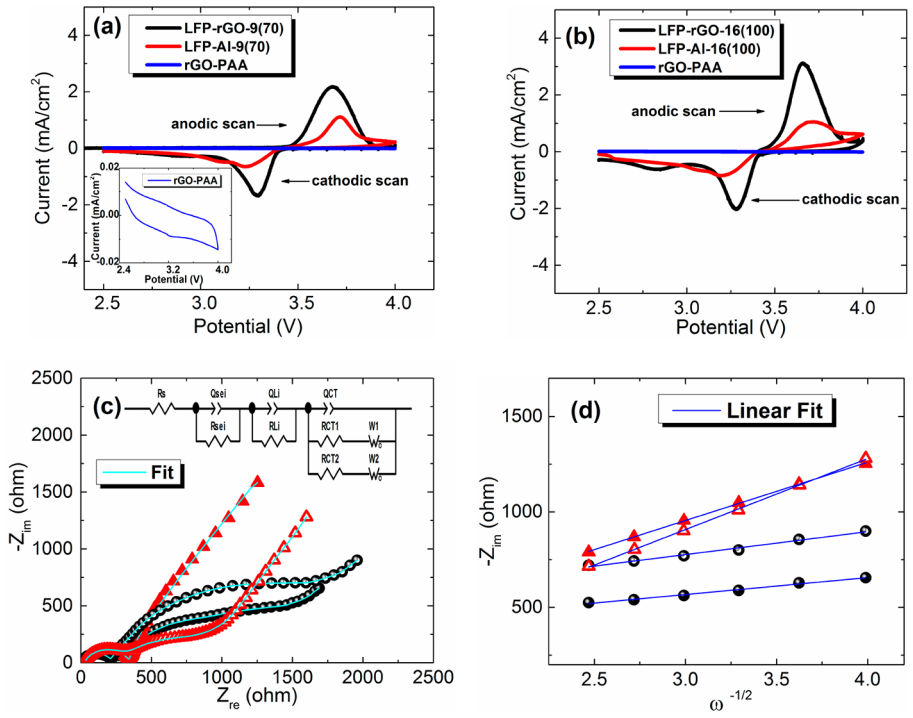

Figure 2. (a) CV of LFP-rGO-9(70) (black trace) and LFP-Al-9(70) (red trace), and pristine rGO-PAA aerogel (blue trace). Inset: zoom-in of peak current passed by rGO-PAA. (b) CV of LFP-rGO-16(100) (black trace), LFP-Al-16(100) (red trace), and rGO-PAA (blue trace). All CV's were performed with a scan rate of 0.1 mV/s. (c) The AC impedance plots of LFP-rGO-9(70) (black spheres), LFP-Al-9(70) (red triangles), LFP-rGO-16(100) (hollow spheres), and LFP-Al-16(100) (hollow triangles). (d) Plots of $-Z_{im}$ versus the reciprocal square root of angular frequency in the low-frequency region obtained from (c). EIS spectra were recorded in the frequency range of 100 kHz−0.01 Hz.

Information. Charge/discharge tests were performed using a multichannel battery test system (BT 2043, Arbin). Cathode materials were assembled in 2032 stainless steel coin cells vs Li foil (Alfa) as the anode. Celgard 2400 membrane (25 μm, Celgard) was used as the cell separator. The electrolyte was composed of 1 M $LiPF_6$ in EC/DEC (1:1 by volume) solution. Excess electrolyte was used (>12 drops) to flood the cell and to provide sufficient electrolyte. Three conditioning C/20 cycles were run for all cells tested to form a consistent SEI prior to commencing galvanostatic charge/discharge tests. For rate capability tests, the cells were run at a C/20 for 3 cycles, C/5 for 5 cycles, C/2 for 5 cycles, 1C for 5 cycles, 2C for 5 cycles, and 5C for 5 cycles and finally recovered at C/5 to examine the capacity retention. For long-term stability tests, all cells were programmed to undergo three C/20 formation cycles followed by long-term cycling at C/5 (200 cycles).

3. RESULTS AND DISCUSSION

3.1. Characterization of the rGO-PAA Substrates Loaded with LFP. Owing to stable discharge voltage, relevance to commercial applications, and long-term cycling stability,[6] a commercially available, high tap density LFP (1.45 ± 0.2 g/cm^3) was selected as the active material for evaluating several three-dimensional rGO-PAA substrates. The tap density of the LFP material used here exceeds that of other commonly used LFP materials (typically ∼1.0−1.2 g/cm^3), which has limited the achievable volumetric energy and power density of these materials. Therefore, enhancing the rate performance and mechanical integrity of LFP electrodes with high density may hasten the utility of LFP in commercial applications.

We found that the aerogel discussed in this work can support a wide range of active material loading including up to 75 mg/cm^2 (for rGO-PAA electrodes with ∼430 μm thickness) while being compressed to less than 1/30 of its original volume (Figure 1a). However, LFP-Al electrodes could not be fabricated at this thickness, and a maximum mass loading of 16 mg/cm^2 (100 μm electrode thickness) with sufficient mechanical integrity was fabricated with the slurry composition used here. It should be noted that very high mass loadings (i.e., ≥50 mg/cm^2) on the rGO-PAA substrate had a lower success rate than with practical mass loadings (10−25 mg/cm^2), likely due to particle delamination and the long Li^+ diffusion distance through the thick electrode architecture. Still, electrodes with a wide range of LFP loading (4−75 mg/cm^2) were electrochemically tested, and some selected data are listed in the Supporting Information (Table S1). This report focuses on two comparable LFP-rGO and LFP-Al electrodes of 9 mg/cm^2 (70 μm thickness) and 16 mg/cm^2 (100 μm thickness) to demonstrate some advantages of the rGO-PAA substrate over the Al foil at commercially relevant mass loadings. The electrodes will be further referred to in the following format: active material-current collector-mass loading (thickness) (e.g., LFP-rGO-9(70) refers to LFP loaded onto rGO-PAA with a mass loading of 9 mg_{LFP}/cm^2 and thickness of ∼70 μm). Figures 1b, 1c, and 1d show the cross-sectional SEM images of a pristine rGO-PAA aerogel with no LFP added, an rGO-PAA aerogel loaded with LFP and Super P Li after drying under slight mechanical pressure, and an rGO-PAA aerogel loaded with LFP and Super P Li calendered to ∼100 μm. With EDS the LFP particles are effectively distributed throughout the cross section (Figure 1e−g and Figure S2).

Both LFP-rGO and LFP-Al electrodes were loaded with 92.5% LFP, 5% Super P, and 2.5% Kraton. Kraton is a poly(styrene-*block*-ethylene/butylene-*block*-styrene) block copolymer, which is an elastic, commercially available thermoplastic elastomer and electrochemically inert battery binder. This specific composition was chosen to minimize the amount

DOI: 10.1021/acsami.7b07283
ACS Appl. Mater. Interfaces 2017, 9, 22641−22651

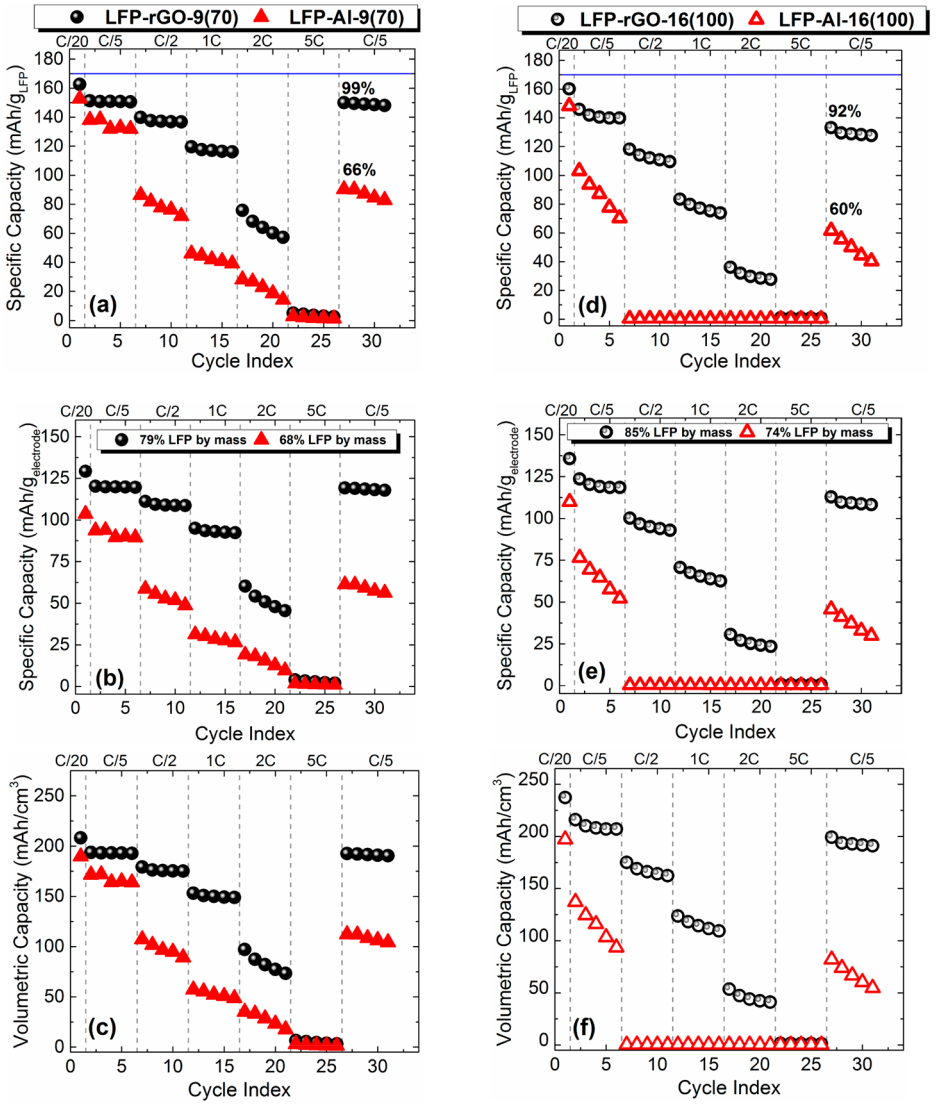

Figure 3. Rate capabilities for LFP-rGO-9(70) (black spheres)/LFP-Al-9(70) (red triangles) (a–c; left column) and LFP-rGO-16(100) (hollow spheres)/LFP-Al-16(100) (hollow triangles) (d–f; right column) demonstrating the active-material specific capacities (a, d), specific capacity per electrode mass (including Super P Li, Kraton, and current collector) (b, e), and volumetric capacities of the composite electrodes (including the current collector) (c, f).

of so-called "inactive components" (i.e., the components that do not directly participate in the cell electrochemistry), while still avoiding potential film delamination and retaining flexibility of the electrode.

3.2. Electrochemical Stability of rGO-PAA Aerogels Tested in LIB. The electrochemical stability of the LFP-rGO was studied using electrochemical impedance spectroscopy (EIS) and cyclic voltammetry (CV). As illustrated in the Figure 2a inset, the pristine aerogel substrate was found to be electrochemically inert over the potential range of 2.5–4.0 V vs Li/Li^+. In the CV traces for both electrode batches (9 and 16 mg/cm^2), the LFP-rGO composite electrodes show improved lithiation/delithiation kinetics compared with LFP-Al electrodes, as evidenced by the higher anodic/cathodic peak currents, increased peak sharpness, and decreased peak separation.[57−59] A second satellite feature appears in the cathodic scan at ~2.8 V for all electrodes tested here and becomes much more significant as the mass loading is increased. This second feature persists for LFP-rGO electrodes until the mass loading and thickness is decreased to ~5 mg/cm^2 and ~40 μm (Figure S3). Since this feature disappears as mass loading and thickness is decreased, we speculate that it arises from kinetic limitations through the thick electrode films, coupled with the large particle size distribution (Figure S2) of LFP commercial particles (D10 < 1.0 μm; D50 = 3.5 ± 1 μm; D90 < 15 μm). This large particle-size distribution causes a highly heterogeneous current distribution through the electrode due to the different lithiation/delithiation kinetics as a function of the Li^+ diffusion distance into the particles. The EIS spectra of all electrodes consist of a superposition of semicircles at the high and medium-frequency regions, followed by an incline in the imaginary component in the low-frequency region (Figure 2c).

The high-frequency semicircle can be attributed to SEI and anode resistances (R_{SEI} and R_{Li}), the medium-frequency semicircle is attributed to the cathode resistance (R_{CT1} and R_{CT2}), and the incline in the low-frequency region represents the Warburg impedance associated with Li^+ diffusion (W_1 and W_2). Figure 2c inset shows the equivalent circuit used to fit the impedance data which was proposed by Osaka et al. to consider a variation in particle size in the cathode.[60] As shown in Figure

DOI: 10.1021/acsami.7b07283
ACS Appl. Mater. Interfaces 2017, 9, 22641−22651

2c, the equivalent circuit fit agrees very well with the experimental data. When adding the two-cathode charge-transfer resistances in parallel, the LFP-rGO-9(70) (223 Ω) and LFP-rGO-16(100) (407 Ω) exhibit reduced $R_{CTtotal}$ values compared to LFP-Al-9(70) (258 Ω) and LFP-Al-16(100) (558 Ω) at similar thickness and mass loading, implying that the rGO-PAA substrate improves the charge transfer and reaction kinetics of the LFP active material.[32] The apparent Li diffusion coefficient (D_{Li}) can be calculated from the incline in the low-frequency region using the following equation:[36]

$$D_{Li} = \frac{1}{2}\left[\left(\frac{V_m}{FSA}\right)\left(\frac{\partial E}{\partial x}\right)\right]^2 \quad (1)$$

where V_m is the molar volume (mol/cm^3), F is Faraday's constant, S is the effective electrode area, $\partial E/\partial x$ is the voltage change upon discharging, where x is the stoichiometry of Li^+ in LFP, and A is the Warburg parameter associated with $-Z_{im}$ ($-Z_{im} \propto A\omega^{-1/2}$). The Warburg parameter can be obtained from the slope of a plot of $-Z_{im}$ against the reciprocal on the angular frequency ($\omega^{-1/2}$) (Figure 2d). The D_{Li} in the LFP-rGO and LFP-Al electrodes is the same since the same LFP powder was used for each electrode preparation, and thus the ratio of the effective LFP surface area in the LFP-rGO and LFP-Al can be obtained by eq 2:[36]

$$r = \frac{S_{LFP\text{-}rGO}}{S_{LFP\text{-}Al}} = \frac{\left(\frac{\partial E}{\partial x}\right)_{LFP\text{-}rGO} A_{LFP\text{-}Al}}{\left(\frac{\partial E}{\partial x}\right)_{LFP\text{-}Al} A_{LFP\text{-}rGO}} \quad (2)$$

for which r = 2 at 9 mg/cm^2 and r = 2.5 at 16 mg/cm^2. By increasing the effective LFP area by 2× and 2.5×, the number of accessible Li^+ intercalation sites is increased for both LFP-rGO electrodes, giving rise to the improved reaction kinetics extracted from the CV and EIS analysis of the LFP-rGO electrodes (Figure 2a–d).

3.3. Application of rGO-PAA Aerogels as Current Collectors for LIB. Galvanostatic charge–discharge tests were used to examine the electrochemical performance of the LFP-Al and LFP-rGO electrodes. Figure 3a illustrates the gravimetric capacity of the LFP-rGO-9(70) and LFP-Al-9(70) electrodes normalized to the mass of LFP loaded onto each electrode. Although both electrodes are overcome by Li^+ and electronic transport limitations at a rate of 5C due to the poor rate capability of the micrometer-sized LFP particles used,[6,15] LFP-rGO-9(70) delivered specific capacities of 163, 151, 140, 119, and 75 mAh/g_{LFP} at C/20, C/5, C/2, 1C, and 2C, respectively. In comparison, the LFP-Al-9(70) delivered capacities of 153, 138, 86, 46, and 26 mAh/g_{LFP} at the same current densities listed previously. While only exhibiting a 7% and 9% capacity increase at C/20 and C/5 over LFP-Al-9(70), the LFP-rGO-9(70) increases the capacity at C/2 and 1C by 39% over LFP-Al-9(70). Desirably, when nearly doubling the LFP loading to 16 mg/cm^2 at ∼100 μm thickness, the LFP-rGO-16(100) electrode demonstrates cycle stability through 2C, whereas the LFP-Al-16(100) is overcome by kinetic limitations at the moderate rate of C/2 (Figure 3d). The LFP-rGO-16(100) delivered specific capacities of 160, 146, 118, 83, and 36 mAh/g_{LFP} at C/20, C/5, C/2, 1C, and 2C, respectively; the LFP-Al-16(100) electrode was only capable of delivering specific capacities of 148 and 103 mAh/g_{LFP} at C/20 and C/5 before becoming unstable and dropping below 1 mAh/g_{LFP} at C/2.

The porous and robust rGO-PAA architecture also facilitates improved LFP-film integrity during cycling, as evidenced by the 33% (Figure 3a) and 32% (Figure 3d) increase in C/5 capacity recovery after completion of the variable-rate tests through 5C. The data presented in Figure 3 demonstrate the promise of using the conductive and porous rGO-PAA current collector to improve the rate performance and mechanical integrity of thicker electrode films with high tap density active materials for LIBs. The performance of the LFP-rGO electrodes reported here compares favorably to those reported by Liu et al., who recently tested the performance of LTO and LFP electrodes on a 3D porous sponge-like PDMS scaffold using sugar cubes as a carbon template.[55] When testing electrodes with an LFP loading of 7 mg/cm^2, the LFP/3D sponge electrodes delivered specific capacities of ∼130 mAh/g at C/5, ∼120 mAh/g at C/2, and ∼110 mAh/g at 1C. Furthermore, the authors noted that the 3D sponge electrodes suffered from particle detachment at active material loadings ≥14 mg/cm^2, and their reported LTO/3D sponge electrode at 14 mg_{LTO}/cm^2 only delivered a specific capacity of 135 mAh/g at a C/10 rate (1 C = 175 mA/g).[55] In comparison, the LFP-rGO-16(100) electrode delivered a specific capacity of 146 mAh/g at nearly twice the current density (C/5; 1 C = 170 mAh/g).

Although the active-material specific capacity is the most commonly reported metric for composite LIB electrodes, the specific capacity per unit mass of electrode (i.e., current collector, polymeric binder, conductive additive) provides a more accurate assessment of a LIB electrode, as the charge-inactive components currently restrict the achievable energy density and increase the cost and volume of LIB cells.[4,6] As illustrated in Figure 3b, the LFP-rGO-9(70) delivers specific capacities increased by 20% at C/20, 22% at C/5, 47% at C/2, 67% at 1C, and 68% at 2C compared to LFP-Al-9(70). Remarkably, LFP-rGO-16(100), with almost double the mass loading, also outperforms the LFP-Al-9(70) electrode by 24% at C/20 and C/5, 42% at C/2, 56% at 1C, and 23% at 2C. This significant improvement is due to the very low density of the rGO-PAA (∼5 mg/cm^3) compared to Al foil (2700 mg/cm^3). The lower density of the rGO-PAA increases the mass fraction of LFP in the LFP-rGO electrodes: LFP accounts for 79% of the mass in LFP-rGO-9(70) and 85% of the mass in LFP-rGO-16(100), while only accounting for 68% in LFP-Al-9(70) and 74% in LFP-Al-16(100).

The LFP-rGO-9(70) and LFP-rGO-16(100) electrodes deliver specific capacities of 120 and 123 mAh/$g_{electrode}$ at C/5 and 95 and 70 mAh/$g_{electrode}$ at 1C, respectively. These results compare well with those reported by Ji et al., who studied the performance of LFP nanoparticles (∼12 mg/cm^2) on an ultrathin graphene foam grown by chemical vapor deposition.[36] In this work, electrodes made without a metal foil current collector performed with reversible capacities of ∼101 mAh/$g_{electrode}$ at C/5 and ∼90 mAh/$g_{electrode}$ at 1C. Notably, three significant differences from the work described here highlight the advantages of the rGO-PAA as an intelligently designed replacement for metal-foil current collectors: (1) Ji et al. reported an average electrode thickness of 1.6 mm, whereas our loaded materials were compressed to a tunable thickness using a calender; (2) although Ji et al. employed nanoscale LFP which should demonstrate improved rate capability due to the higher surface area and reduced Li^+ diffusion distance,[15] the LFP-rGO electrodes discussed here with micrometer-sized LFP particles perform very competitively at rates up to 1C; and (3) although not directly reported, the electrode density and

DOI: 10.1021/acsami.7b07283
ACS Appl. Mater. Interfaces 2017, 9, 22641–22651

volumetric capacities of the electrodes reported by Ji et al. should be quite low due to the low density of LFP particles dispersed throughout the very thick graphene-foam current collector.

Owing to the dispersed LFP particles throughout the porous 3-D architecture of the rGO-PAA substrate (Figure 1c,d and Figure S4), the volume and mass occupied by LFP is increased in the LFP-rGO electrodes. In contrast, conventional electrodes suffer from a charge-empty space occupied by the metal foil current collector which reduces the total volume that LFP occupies and thus limits the overall volumetric energy density for the LFP-Al electrodes (Figure 3c,f). The active-material densities in the LFP-rGO electrodes were also exceptionally high, with the LFP-rGO-9(70) at 1.4 g/cm^3 and the LFP-rGO-16(100) at 1.6 g/cm^3. In comparison, the LFP-Al-9(70) and LFP-Al-16(100) had slightly lower densities of 1.2 and 1.3 g/cm^3, respectively. These data demonstrate the prospect of the rGO-PAA scaffold to increase the volume and mass occupied by the active material while also improving the mechanical stability and rate performance of thick electrode films without significantly increasing production costs (fabricated from inexpensive graphite and PAA) or altering industrially adopted processing methods.

Figure 4 illustrates the first galvanostatic charge/discharge cycle at C/20 for LFP-rGO and LFP-Al-electrodes. Both LFP-rGO electrodes showed a flat discharge plateau at ~3.40 V, which is characteristic of LFP and indicates that the two-phase redox transition proceeds via a first-order transition between

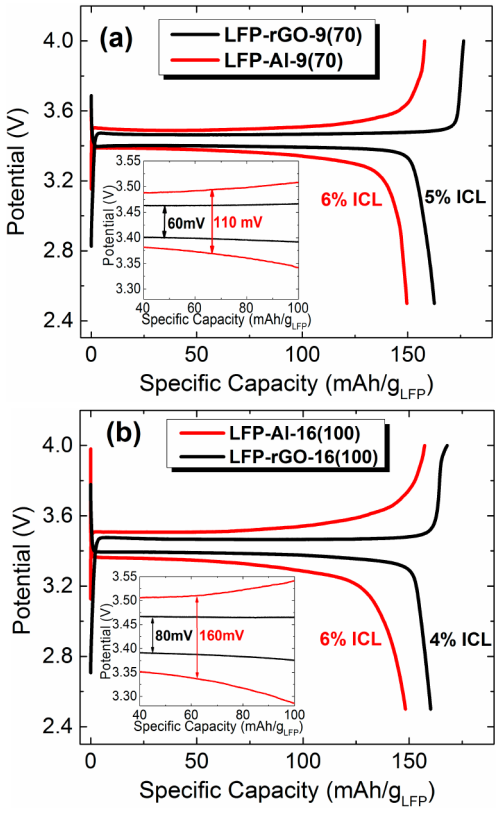

Figure 4. First galvanostatic charge/discharge profile at C/20 for (a) LFP-rGO-9(70) (black trace) and LFP-Al-9(70) (red trace) and (b) LFP-rGO-16(100) (black trace) and LFP-Al-16(100) (red trace). Galvanostatic charge−discharge tests were conducted in the potential window of 2.5−4.0 V vs Li/Li$^+$.

$FePO_4$ and $LiFePO_4$.[32,56,57] In contrast, the LFP-Al electrodes show discharge plateaus at 3.37 and 3.35 V for LFP-Al-9(70) and LFP-Al-16(100), respectively, due to the inherently poor transport kinetics of LFP. As demonstrated in Figure 4, the LFP-rGO electrodes exhibit a higher initial discharge capacity, a slightly lower irreversible capacity loss (ICL), and ~50% reduced potential gap between charge/discharge plateaus for both the 9 mg/cm^2 (Figure 4a inset) and 16 mg/cm^2 (Figure 4b inset) electrodes.

The roughly 50% reduction in the potential gap between charge/discharge plateaus supports the CV and EIS data (Figure 2a−c) and indicates that the LFP-rGO electrodes exhibit improved lithiation/delithiation kinetics and lower polarization than the LFP-Al electrodes due to the increased effective LFP surface area induced by the rGO-PAA substrate.

To examine the cycle stability of the rGO-PAA current collector, long-term cycling tests were conducted at C/5 for both LFP-rGO and LFP-Al electrodes. As shown in Figures 5a and 5b, the LFP-rGO-9(70) and LFP-rGO-16(100) show improved specific capacities and capacity retention over 200 cycles; this stability test consisting of 200 cycles is similar to other reports of free-standing 3-D current collectors in LIBs.[34,36−41] It is important to note that all the electrodes tested here demonstrated relatively high capacity fade due to the thick electrode films; after 200 cycles, capacity loss of 17% 25%, 37%, and >99% were observed for LFP-rGO-9(70), LFP-rGO-16(100), LFP-Al-9(70), and LFP-Al-16(100), respectively. Although the robust rGO-PAA scaffold mitigates LFP delamination during cycling, the large capacity fade is attributed to the broad particle size distribution of the commercial LFP particles (Figure S2) that display significantly different lithiation/delithiation kinetics and cause a heterogeneous current distribution within the electrode leading to the relatively high capacity fade over 200 cycles (Figure 5a,b).[58] This justification is supported by the high and steady Coulombic efficiency values demonstrated by LFP-rGO-9(70) (~98−99% following initial C/5 cycle) and LFP-Al-9(70) (~97−98% following initial C/5 cycle). When increasing the mass loading to 16 mg/cm^2, the LFP-rGO electrode exhibits a more significant initial decrease in capacity compared to the LFP-rGO-9(70), as expected due to the increase in electrode thickness and density.[4,16] The LFP-rGO-16(100) appears to follow the same proposed diffusion-limited/broad particle-size capacity fade mechanism, as evidenced by the high and consistent Coulombic efficiency values (~97−98% following the initial C/5 cycle). In contrast, the LFP-Al-16(100) electrode suffers from significant capacity loss and poor Coulombic efficiency (84−89%) throughout the first ~80 cycles before becoming unstable, as indicated by the Coulombic efficiency values reaching above 100% and the reversible capacity dropping to ~1 mAh/g. This poor cycling behavior in the first ~80 cycles indicates significant mechanical integrity issues of the LFP-Al-16(100) electrode that results in considerable particle delamination from the current collector surface and a large loss in capacity.[61]

Of the published free-standing current collector studies (i.e., no metal-foil current collector),[34,36−41,55] we are aware of only one study that reports cycle stability for at least 200 cycles with an active-material loading of ≥9 mg/cm^2. In this work, Wang et al. fabricated a nitrogen−sulfur doped 3-D carbon paper/porous carbon host electrode in a Li/S cell.[41] Electrodes with 9 mg$_{Sulfur}$/cm^2 retained 85% of their initial C/4 capacity after 200 cycles (0.074% capacity fade per cycle). However, without the

DOI: 10.1021/acsami.7b07283
ACS Appl. Mater. Interfaces 2017, 9, 22641−22651

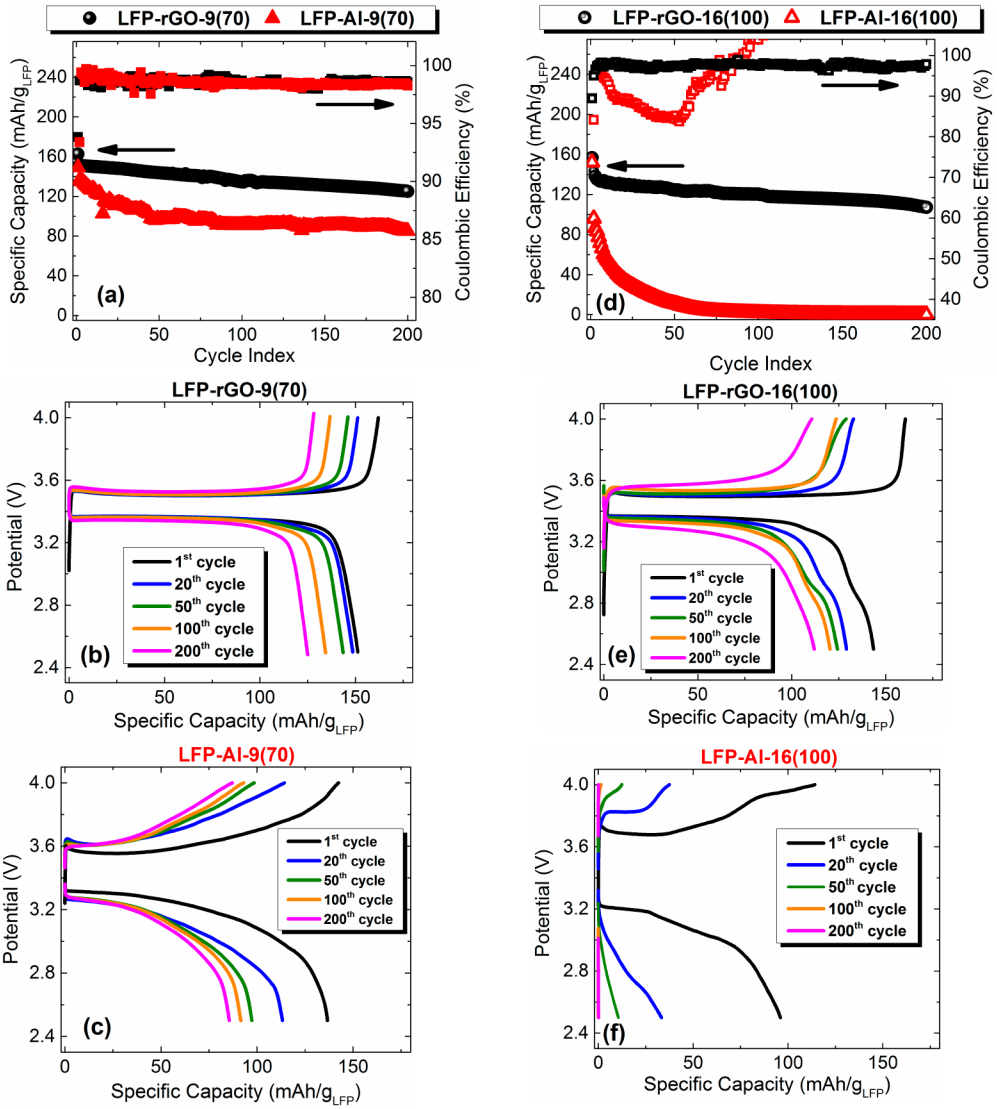

Figure 5. Cycle stability tests of the LFP-rGO and LFP-Al electrodes at 9 mg/cm^2 (a–c) and 16 mg/cm^2 (d–f) at a C/5 rate. (a, d) Left axis: cycling performance over 200 cycles for LFP-rGO-9(70) (black sphere)/LFP-Al-9(70) (red triangle) (a) and LFP-rGO-16(100) (hollow sphere)/LFP-Al-16(100) (hollow triangle) (d). Right axis: Coulombic efficiency values for 200 cycles at C/5 for LFP-rGO-9(70) (black square)/LFP-Al-9(70) (red square) (a) and LFP-rGO-16(100) (hollow square)/LFP-Al-16(100) (hollow square) (d). The first data point represents the discharge capacity at C/20. Galvanostatic charge–discharge profiles collected at different cycles for LFP-rGO-9(70) (b) LFP-Al-9(70) (c), LFP-rGO-16(100) (e), and LFP-Al-16(100) (f).

N and S codoping, the carbon paper/porous carbon composite displayed significant capacity fade and retained only 53% of its initial capacity after 168 cycles. After 168 cycles, the capacity suddenly decreased to almost zero, likely due to increased reaction of polysulfide with the Li-metal anode and breakdown of the composite structure.[41] Without the addition of any dopants, the LFP-rGO-9(70) and LFP-rGO-16(100) electrodes compare favorably to the pristine carbon paper used by Wang et al., achieving 83% and 75% recovery of the initial specific capacity after 200 cycles. The other studies aimed at replacing conventional metal foil electrodes either employed a low mass loading (≤6 mg/cm^2) did not directly report a mass loading or only provided cycle stability up to ~60 cycles.[34,36−40,55] Thus, these works are not as relevant to the electrodes with high active-material loadings discussed here.

The improved stability of the composite electrodes made by the rGO-PAA substrate is clearly reflected in the galvanostatic charge–discharge profiles collected after the first, 20th, 50th, 100th, and 200th cycle at a C/5 rate. In comparison to the LFP-Al electrodes, the LFP-rGO electrodes exhibit higher specific capacities and steadier charge–discharge plateaus due to the enhanced Li^+-diffusion in the LFP-rGO electrodes facilitated by the increased LFP/electrolyte contact area (Figure 5b,c,e,f). Consistent with the CV traces for LFP-Al-9, LFP-Al-16, and LFP-rGO-16 (Figure 2a,b), a second feature appears in the charge/discharge profiles, suggesting that an increase electrode density and thickness magnifies the difference in lithiation/delithiation kinetics for the broad LFP particle distribution used here.[56−58,61] Still, the rate performance, cycle stability, and mechanical durability of the LFP-rGO electrodes demonstrate the prospects of the rGO-PAA current collector to facilitate improvements in the performance of thick LIB electrodes.

DOI: 10.1021/acsami.7b07283
ACS Appl. Mater. Interfaces 2017, 9, 22641−22651

4. CONCLUSIONS

A highly elastic, mechanically robust rGO-PAA aerogel was tested as a three-dimensional substitute for a conventional Al-foil current collector. The aerogel's low density, highly porous and tunable carbon framework, ability to accommodate high areal/volumetric active material (LFP) loading, and ability to withstand compression lend the rGO-PAA as an attractive current collector for LIBs. Electrochemical metrics were obtained for rGO-PAA aerogel electrodes and compared to analogues composed of Al-foil at 9 mg/cm^2 (~70 μm thickness) and 16 mg/cm^2 (~100 μm thickness). The difficulty in making and handling thick electrode films that are conventionally cast on metal foils is overcome by using the flexible and porous aerogel, rendering LFP-rGO electrodes more mechanically robust than LFP-Al. In comparison to LFP-Al electrodes, the LFP-rGO electrodes increased the electrode-specific capacity and volumetric capacity by 68% and 63%, respectively. Furthermore, long-term stability tests at a charge/discharge rate of C/5 demonstrated increased specific capacities and lower capacity fade after 200 cycles for the LFP-rGO electrodes. From these data, the rGO-PAA aerogel shows promise as an alternative current collector for enhancing the performance of thick films composed of high-tap density electrodes by increasing effective electroactive surface area (2× at 9 mg/cm^2 and 2.5× at 16 mg/cm^2). Looking ahead, its application does not end at lithium-ion cathodes. Because of the highly porous structure, this substrate can also be used for LIB anodes, and the materials and methods proposed in this work can be further extended and applied to different active materials to further improve cycling performance and capacities. The 3-D scaffold not only provides sufficient space for active and inactive components of the cell but also allows viscous electrolytes (such as those being used in Li−S batteries that use solvent in salt or "solvate" type electrolytes) to permeate through the electrodes more quickly, which increases the rate of ion transport. Through manipulation of the rGO-PAA synthesis and processing methods to tune the substrate's pore morphology and surface chemistry for optimized current collector properties, we anticipate maturing the rGO-PAA scaffold to help address issues with film integrity and kinetic limitations that currently plague thick electrode films.

■ ASSOCIATED CONTENT

Supporting Information

The Supporting Information is available free of charge on the ACS Publications website at DOI: 10.1021/acsami.7b07283.

Calculating the mass percent of active material on the whole cathode (including current collector) from Ji et al. and MTI Corporation; a brief procedure for synthesizing LFP-rGO; selected cell capacities of electrodes with different LFP mass loadings; SEM images of commercial LFP particles used in this study; cross-sectional SEM image of LFP-rGO showing effective particle distribution along cross section; CV curves of LFP-rGO electrodes at different mass loadings; $I-V$ curves from 4-point probe measurements; top-down SEM image of the rGO-PAA electrode after one discharge cycle; summary of experimental highlights (PDF)

■ AUTHOR INFORMATION

Corresponding Authors

*(C.B.M.) E-mail mullins@che.utexas.edu.

*(C.J.E.) E-mail cellison@umn.edu.

ORCID

Christopher J. Ellison: 0000-0002-0393-2941

C. Buddie Mullins: 0000-0003-1030-4801

Author Contributions

H.X. and J.P.P. contributed equally.

Notes

The authors declare no competing financial interest.

■ ACKNOWLEDGMENTS

The authors gratefully acknowledge the Welch Foundation for support of this work (AH-grant F-1131, CJE-grant F-1709, CBM-grant F-1436). C.B.M. is also grateful to the National Science Foundation for support (grant# CBET-1603491). We also thank Celgard for providing membrane separators and Kraton polymer for providing Kraton. We also thank M. Meyerson, S. Nathan, J. Miller, M. Nuschke, and B. Wygant for their contributions regarding making of electrolytes and coin cells as well as performing some electrochemical tests.

■ REFERENCES

(1) Tarascon, J. M.; Armand, M. Issues and Challenges Facing Rechargeable Lithium Batteries. *Nature* **2001**, *414*, 359−367.

(2) Dunn, B.; Kamath, H.; Tarascon, J. M. Electrical Energy Storage for the Grid: A Battery of Choices. *Science* **2011**, *334*, 928−935.

(3) Lu, L.; Han, X.; Li, J.; Hua, J.; Ouyang, M. A Review on the Key Issues for Lithium-Ion Battery Management in Electric Vehicles. *J. Power Sources* **2013**, *226*, 272−288.

(4) Wood, D. L.; Li, J.; Daniel, C. Prospects for Reducing the Processing Cost of Lithium Ion Batteries. *J. Power Sources* **2015**, *275*, 234−242.

(5) Goodenough, J. B.; Park, K. S. The Li-Ion Rechargeable Battery: A Perspective. *J. Am. Chem. Soc.* **2013**, *135*, 1167−1176.

(6) Andre, D.; Kim, S. J.; Lamp, P.; Lux, S. F.; Maglia, F.; Paschos, O.; Stiaszny, B. Future Generations of Cathode Materials: An Automotive Industry Perspective. *J. Mater. Chem. A* **2015**, *3*, 6709−6732.

(7) Zhang, W. J. Structure and Performance of $LiFePO_4$ Cathode Materials: A Review. *J. Power Sources* **2011**, *196*, 2962−2970.

(8) Zhang, W. J. Comparison of the Rate Capacities of $LiFePO_4$ Cathode Materials. *J. Electrochem. Soc.* **2010**, *157*, A1040−A1046.

(9) Kang, B.; Ceder, G. Battery Materials for Ultrafast Charging and Discharging. *Nature* **2009**, *458*, 190−193.

(10) Choi, D.; Wang, D.; Viswanathan, V. V.; Bae, I. T.; Wang, W.; Nie, Z.; Zhang, J. G.; Graff, G. L.; Liu, J.; Yang, Z.; Duong, T. Li-Ion Batteries from $LiFePO_4$ Cathode and Anatase/Graphene Composite Anode for Stationary Energy Storage. *Electrochem. Commun.* **2010**, *12*, 378−381.

(11) Wang, G.; Liu, H.; Liu, J.; Qiao, S.; Lu, G. M.; Munroe, P.; Ahn, H. Mesoporous $LiFePO_4$/C Nanocomposite Cathode Materials for High Power Lithium Ion Batteries with Superior Performance. *Adv. Mater.* **2010**, *22*, 4944−4948.

(12) Malik, R.; Burch, D.; Bazant, M.; Ceder, G. Particle Size Dependence of the Ionic Diffusivity. *Nano Lett.* **2010**, *10*, 4123−4127.

(13) Zane, D.; Carewska, M.; Scaccia, S.; Cardellini, F.; Prosini, P. P. Factor Affecting Rate Performance of Undoped $LiFePO_4$. *Electrochim. Acta* **2004**, *49*, 4259−4271.

(14) Doeff, M. M.; Hu, Y.; McLarnon, F.; Kostecki, R. Effect of Surface Carbon Structure on the Electrochemical Performance of $LiFePO_4$. *Electrochem. Solid-State Lett.* **2003**, *6*, A207−A209.

(15) Sun, C.; Rajasekhara, S.; Goodenough, J. B.; Zhou, F. Monodisperse Porous $LiFePO_4$ Microspheres for a High Power Li-Ion Battery Cathode. *J. Am. Chem. Soc.* **2011**, *133*, 2132−2135.

(16) Zheng, H.; Li, J.; Song, X.; Liu, G.; Battaglia, V. S. A Comprehensive Understanding of Electrode Thickness Effects on the

DOI: 10.1021/acsami.7b07283
ACS Appl. Mater. Interfaces 2017, 9, 22641−22651

Electrochemical Performances of Li-Ion Battery Cathodes. *Electrochim. Acta* **2012**, *71*, 258−265.
(17) Nan, C.; Lu, J.; Li, L.; Li, L.; Peng, Q.; Li, Y.; Size. and Shape Control of $LiFePO_4$ Nanocrystals for Better Lithium Ion Battery Cathode Materials. *Nano Res.* **2013**, *6*, 469−477.
(18) Kim, H.; Kim, H.; Kim, S. W.; Park, K. Y.; Kim, J.; Jeon, S.; Kang, K. Nano-Graphite Platelet Loaded with $LiFePO_4$ Nanoparticles Used as the Cathode in a High Performance Li-Ion Battery. *Carbon* **2012**, *50*, 1966−1971.
(19) Wang, B.; Wang, D.; Wang, Q.; Liu, T.; Guo, C.; Zhao, X. Improvement of the Electrochemical Performance of Carbon-Coated $LiFePO_4$ Modified with Reduced Graphene Oxide. *J. Mater. Chem. A* **2013**, *1*, 135−144.
(20) Hu, L. H.; Wu, F. Y.; Lin, C. T.; Khlobystov, A. N.; Li, L. J. Graphene-Modified $LiFePO_4$ Cathode for Lithium Ion Battery Beyond Theoretical Capacity. *Nat. Commun.* **2013**, *4*, 1687.
(21) Oh, S. W.; Myung, S. T.; Bang, H. J.; Yoon, C. S.; Amine, K.; Sun, Y. K. Nanoporous Structured $LiFePO_4$ with Spherical Microscale Particles Having High Volumetric Capacity for Lithium Batteries. *Electrochem. Solid-State Lett.* **2009**, *12*, A181−A185.
(22) Gu, W.; Yushin, G. Review of Nanostructured Carbon Materials for Electrochemical Capacitor Applications: Advantages and Limitations of Activated Carbon, Carbide-Derived Carbon, Zeolite-Templated Carbon, Carbon Aerogels, Carbon Nanotubes, Onion-like Carbon, and Graphene. *Wiley Interdiscip. Rev.: Energy Environ.* **2014**, *3*, 424−473.
(23) Ambrosi, A.; Chua, C. K.; Bonanni, A.; Pumera, M. Electrochemistry of Graphene and Related Materials. *Chem. Rev.* **2014**, *114*, 7150−7188.
(24) Wang, H.; Feng, H.; Li, J. Graphene and Graphene-Like Layered Transition Metal Dichalcogenides in Energy Conversion and Storage. *Small* **2014**, *10*, 2165−2181.
(25) Mahmood, N.; Zhang, C.; Yin, H.; Hou, Y. Graphene-Based Nanocomposites for Energy Storage and Conversion in Lithium Batteries, Supercapacitors and Fuel Cells. *J. Mater. Chem. A* **2014**, *2*, 15−32.
(26) Zhu, J.; Yang, D.; Yin, Z.; Yan, Q.; Zhang, H. Graphene and Graphene-Based Materials for Energy Storage Applications. *Small* **2014**, *10*, 3480−3498.
(27) Xu, C.; Xu, B.; Gu, Y.; Xiong, Z.; Sun, J.; Zhao, X. S. Graphene-Based Electrodes for Electrochemical Energy Storage. *Energy Environ. Sci.* **2013**, *6*, 1388−1414.
(28) Vlad, A.; Singh, N.; Galande, C.; Ajayan, P. M. Design Considerations for Unconventional Electrochemical Energy Storage Architectures. *Adv. Energy Mater.* **2015**, *5*, 1402115.
(29) Su, F. Y.; You, C.; He, Y. B.; Lv, W.; Cui, W.; Jin, F.; Li, B.; Yang, Q. H.; Kang, F. Flexible and Planar Graphene Conductive Additives for Lithium-Ion Batteries. *J. Mater. Chem.* **2010**, *20*, 9644−9650.
(30) Rao, C. V.; Reddy, A. L. M.; Ishikawa, Y.; Ajayan, P. M. Synthesis and Electrocatalytic Oxygen Reduction Activity of Graphene-Supported Pt_3Co and Pt_3Cr Alloy Nanoparticles. *Carbon* **2011**, *49*, 931−936.
(31) Ji, J.; Ji, H.; Zhang, L. L.; Zhao, X.; Bai, X.; Fan, X.; Zhang, F.; Ruoff, R. S. Graphene-Encapsulated Si on Ultrathin-Graphite Foam as Anode for High Capacity Lithium-Ion Batteries. *Adv. Mater.* **2013**, *25*, 4673−4677.
(32) Tian, X.; Zhou, Y.; Tu, X.; Zhang, Z.; Du, G. Well-Dispersed $LiFePO_4$ Nanoparticles Anchored on a Three-Dimensional Graphene Aerogel as High-Performance Positive Electrode Materials for Lithium-ion Batteries. *J. Power Sources* **2017**, *340*, 40−50.
(33) Chen, Z.; Ren, W.; Gao, L.; Liu, B.; Pei, S.; Cheng, H. M. Three-Dimensional Flexible and Conductive Interconnected Graphene Networks Grown by Chemical Vapour Deposition. *Nat. Mater.* **2011**, *10*, 424−428.
(34) Zhou, G.; Paek, E.; Hwang, G. S.; Manthiram, A. Long-Life Li/Polysulphide Batteries with High Sulphur Loading Enabled by Lightweight Three-Dimensional Nitrogen/Sulphur-Codoped Graphene Sponge. *Nat. Commun.* **2015**, *6*, 7760.
(35) Ha, H.; Shanmuganathan, K.; Ellison, C. J. Mechanically Stable Thermally Crosslinked Poly(acrylic acid)/Reduced Graphene Oxide Aerogels. *ACS Appl. Mater. Interfaces* **2015**, *7*, 6220−6229.
(36) Ji, H.; Zhang, L.; Pettes, M. T.; Li, H.; Chen, S.; Shi, L.; Piner, R.; Ruoff, R. S. Ultrathin Graphite Foam: A Three-Dimensional Conductive Network for Battery Electrodes. *Nano Lett.* **2012**, *12*, 2446−2451.
(37) He, J.; Chen, Y.; Lv, W.; Wen, K.; Li, P.; Qi, F.; Wang, Z.; Zhang, W.; Li, Y.; Qin, W.; He, W. Highly-Flexible 3D Li_2S/Graphene Cathode for High-Performance Lithium Sulfur Batteries. *J. Power Sources* **2016**, *327*, 474−480.
(38) Fan, C. Y.; Liu, S. Y.; Li, H. H.; Wang, H. F.; Wang, H. C.; Wu, X. L.; Sun, H. Z.; Zhang, J. P. Synergistic Design of Cathode Region for the High-Energy-Density Li-S Batteries. *ACS Appl. Mater. Interfaces* **2016**, *8*, 28689−28699.
(39) Mentbayeva, A.; Belgibayeva, A.; Umirov, N.; Zhang, Y.; Taniguchi, I.; Kurmanbayeva, I.; Bakenov, Z. High Performance Freestanding Composite Cathode for Lithium-Sulfur Batteries. *Electrochim. Acta* **2016**, *217*, 242−248.
(40) Du, Y.; Tang, Y.; Huang, F.; Chang, C. Preparation of Three-Dimensional Free-Standing Nano-$LiFePO_4$/Graphene Composite for High Performance Lithium-Ion Battery. *RSC Adv.* **2016**, *6*, 52279−52283.
(41) Wang, X.; Gao, T.; Han, F.; Ma, Z.; Zhang, Z.; Li, J.; Wang, C. Stabilizing High Sulfur Loading Li−S Batteries by Chemisorption of Polysulfide on Three-Dimensional Current Collector. *Nano Energy* **2016**, *30*, 700−708.
(42) Liu, N.; Shen, J.; Liu, D. A Fe_2O_3 Nanoparticle/Carbon Aerogel Composite for Use as an Anode Material for Lithium Ion Batteries. *Electrochim. Acta* **2013**, *97*, 271−277.
(43) Yin, L.; Zhang, Z.; Li, Z.; Hao, F.; Li, Q.; Wang, C.; Fan, R.; Qi, Y. Spinel $ZnMn_2O_4$ Nanocrystal-Anchored 3D Hierarchical Carbon Aerogel Hybrids as Anode Materials for Lithium Ion Batteries. *Adv. Funct. Mater.* **2014**, *24*, 4176−4185.
(44) Hao, F.; Zhang, Z.; Yin, L. Co_3O_4/Carbon Aerogel Hybrids as Anode Materials for Lithium-Ion Batteries with Enhanced Electrochemical Properties. *ACS Appl. Mater. Interfaces* **2013**, *5*, 8337−8344.
(45) Yang, X.; Huang, H.; Zhang, G.; Li, X.; Wu, D.; Fu, R. Carbon Aerogel with 3-D Continuous Skeleton and Mesopore Structure for Lithium-Ion Batteries Application. *Mater. Chem. Phys.* **2015**, *149−150*, 657−662.
(46) Zhang, Z.; Jiang, S.; Lai, Y.; Li, J.; Song, J.; Li, J. Selenium Sulfide@Mesoporous Carbon Aerogel Composite for Rechargeable Lithium Batteries with Good Electrochemical Performance. *J. Power Sources* **2015**, *284*, 95−102.
(47) Zhang, H.; Liu, D.; Qian, X.; Zhao, C.; Xu, Y. A Novel Nano Structured $LiFePO_4$/C Composite as Cathode for Li-Ion Batteries. *J. Power Sources* **2014**, *249*, 431−434.
(48) Zhou, J.; Liu, B. H.; Li, Z. P. Nanostructure Optimization of $LiFePO_4$/Carbon Aerogel Composites for Performance Enhancement. *Solid State Ionics* **2013**, *244*, 23−29.
(49) Balakumar, K.; Kalaiselvi, N. High Sulfur Loaded Carbon Aerogel Cathode for Lithium−Sulfur Batteries. *RSC Adv.* **2015**, *5*, 34008−34018.
(50) He, Y.; Fu, Z.; Zhou, Q.; Zhong, M.; Yuan, L.; Wei, J.; Yang, X.; Wang, C.; Zeng, Y. Fabrication and Electrochemical Behavior of a Lithium-Sulfur Cell with a TiO_2-Sulfur-Carbon Aerogel-Based Cathode. *Ionics* **2015**, *21*, 3065−3073.
(51) Li, X.; Pan, L.; Wang, Y.; Xu, C. High Efficiency Immobilization of Sulfur on Ce-Doped Carbon Aerogel for High Performance Lithium-Sulfur Batteries. *Electrochim. Acta* **2016**, *190*, 548−555.
(52) Xu, D. W.; Xin, S.; You, Y.; Li, Y.; Cong, H. P.; Yu, S. H. Built-in Carbon Nanotube Network inside a Biomass-Derived Hierarchially Porous Carbon to Enhance the Performance of the Sulfur Cathode in a Li-S Battery. *ChemNanoMat* **2016**, *2*, 712−718.
(53) Xin, S.; Yu, L.; You, Y.; Cong, H. P.; Yin, Y. X.; Du, X. L.; Guo, Y. G.; Yu, S. H.; Cui, Y.; Goodenough, J. B. The Electrochemistry with Lithium Versus Sodium of Selenium Confined To Slit Micropores in Carbon. *Nano Lett.* **2016**, *16*, 4560−4568.

DOI: 10.1021/acsami.7b07283
ACS Appl. Mater. Interfaces 2017, 9, 22641−22651

(54) Yin, Y. X.; Xin, S.; Guo, Y. G.; Wan, L. J. Lithium Sulfur Batteries: Electrochemistry, Materials, and Prospects. *Angew. Chem., Int. Ed.* **2013**, *52*, 13186−13200.
(55) Liu, W.; Chen, Z.; Zhou, G.; Sun, Y.; Lee, H. R.; Liu, C.; Yao, H.; Bao, Z.; Cui, Y. 3D Porous Spong-Inspired Electrode for Stretchable Lithium-Ion Batteries. *Adv. Mater.* **2016**, *28*, 3578−3583.
(56) Fan, C. Y.; Yuan, H. Y.; Li, H. H.; Wang, H. F.; Li, W. L.; Sun, H. Z.; Wu, X. L.; Zhang, J. P. The Effective Design of a Polysulfide-Trapped Separator at the Molecular Level for High Energy Density Li-S Batteries. *ACS Appl. Mater. Interfaces* **2016**, *8*, 16108−16115.
(57) Liu, X.; Huang, J. Q.; Zhang, Q.; Liu, X. Y.; Peng, H. J.; Zhu, W.; Wei, F. N-Methyl-2-Pyrrolidone-Assisted Solvothermal Synthesis of Nanosize Orthorhombic Lithium Iron Phosphate with Improved Li-Storage Performance. *J. Mater. Chem.* **2012**, *22*, 18908−18914.
(58) Gu, Y.; Liu, W.; Wang, L.; Li, G.; Yang, Y. Synthesis of 3D-Hiearchical $LiMPO_4$ (M = Fe, Mn) Microstructures as Cathode Materials for Lithium-Ion Batteries. *CrystEngComm* **2013**, *15*, 4865−4870.
(59) Yu, D. Y. W.; Fietzek, C.; Weydanz, W.; Donoue, K.; Inoue, T.; Kurokawa, H.; Fujitani, S. Study of $LiFePO_4$ by Cyclic Voltammetry. *J. Electrochem. Soc.* **2007**, *154*, A253−A257.
(60) Osaka, T.; Momma, T.; Mukoyama, D.; Nara, H. Proposal of Novel Equivalent Circuit for Electrochemical Impedance Analysis of Commercially Available Lithium Ion Battery. *J. Power Sources* **2012**, *205*, 483−486.
(61) Delacourt, C.; Poizot, P.; Levasseur, S.; Masquelier, C. Size Effects on Carbon-Free $LiFePO_4$ Powders. *Electrochem. Solid-State Lett.* **2006**, *9*, A352−A355.

DOI: 10.1021/acsami.7b07283
ACS Appl. Mater. Interfaces 2017, 9, 22641−22651